Atmos. Chem. Phys., 5, 153–167, 2005
www.atmos-chem-phys.org/acp/5/153/
SRef-ID: 1680-7324/acp/2005-5-153
European Geosciences Union

Atmospheric Chemistry and Physics

# Subtropical trace gas profiles determined by ground-based FTIR spectroscopy at Izaña (28° N, 16° W): Five-year record, error analysis, and comparison with 3-D CTMs

**M. Schneider**[1], **T. Blumenstock**[1], **M. P. Chipperfield**[2], **F. Hase**[1], **W. Kouker**[1], **T. Reddmann**[1], **R. Ruhnke**[1], **E. Cuevas**[3], **and H. Fischer**[1]

[1]IMK-ASF, Forschungszentrum Karlsruhe, Karlsruhe, Germany
[2]Institute for Atmospheric Science, University of Leeds, Leeds, UK
[3]Observatorio Atmosférico de Izaña, Instituto Nacional de Meteorología, Spain

Received: 2 April 2004 – Published in Atmos. Chem. Phys. Discuss.: 8 September 2004
Revised: 12 January 2005 – Accepted: 14 January 2005 – Published: 24 January 2005

**Abstract.** Within the framework of the NDSC (Network for the Detection of Stratospheric Change) ground-based FTIR solar absorption spectra have been routinely recorded at Izaña Observatory (28° N, 16° W) on Tenerife Island since March 1999. By analyzing the shape of the absorption lines, and their different temperature sensitivities, the vertical distribution of the absorbers can be retrieved. Unique time series of subtropical profiles of $O_3$, HCl, HF, $N_2O$, and $CH_4$ are presented. The effects of both dynamical and chemical annually varying trace gas cycles can be seen in the retrieved profiles. These include enhanced upwelling and photochemistry in summer and a more disturbed atmosphere in winter, which are typical of the subtropical stratosphere. A detailed error analysis has been performed for each profile. The output from two different three-dimensional (3-D) chemical transport models (CTMs), which are forced by ECMWF analyses, are compared to the measured profiles. Both models agree well with the measurements in tracking abrupt variations in the atmospheric structure, e.g. due to tropical streamers, in particular for the lower stratosphere. Simulated and measured profiles also reflect similar dynamical and chemical annual cycles. However, the differences between their mixing ratios clearly exceed the error bars estimated for the measured profiles. Possible reasons for this are discussed.

## 1 Introduction

During the last two decades our scientific understanding of chemical and dynamical processes within the stratosphere has improved significantly. Nevertheless, the current state of knowledge still does not permit models to simulate, for example, the observed ozone depletion quantitatively (e.g. European Union, 2001). In the tropics, where the majority of transport from the troposphere into the stratosphere occurs through the upwelling branch of the large-scale circulation (Brewer, 1949; Dobson, 1956), the conversion of anthropogenic gases into reactive compounds is very efficient through enhanced photochemistry. A better knowledge of the timescales of chemical and transport processes within the tropics, and in particular across the so-called subtropical transport barrier (e.g. Trepte and Hitchman, 1992), should thus improve our understanding of the stratosphere globally. An essential requirment for a detailed study of these mechanisms are continuous observations of the current state of the stratosphere, e.g. in the form of atmospheric trace gas profiles which contain information on chemical and dynamical processes. Comparison of measured trace gas profiles with models, which represent chemistry and transport in three dimensions (3-D CTMs), are therefore well-suited to test if the processes assumed in the model agree with the behaviour of the real atmosphere.

Profile data for low latitudes are far less abundant than for middle or high latitudes. In fact, before 1999 only data from ozone soundings and satellite measurements were available on a continuous basis. Ozone is a chemically active species, and hence cannot be used unambiguously to distinguish between chemical and dynamical processes. Satellite data are limited to the lifetime of the satellite instrument and depend on additional validation measurements. Ground-based FTIR solar absorption spectroscopy allows us to determine a large variety of atmospheric trace gas profiles simultaneously. The possibility to access the experimental setup whenever necessary, allows to verify and document the quality of

*Correspondence to:* M. Schneider
(matthias.schneider@imk.fzk.de)

**Table 1.** Applied microwindows and additional constraints.

| Gas | Windows [$cm^{-1}$] | Fixed to a-priori | Interfering gases |
|---|---|---|---|
| $O_3$ | 782.5–782.7<br>788.8–789.4 | surface +80 km | $H_2O$, $CO_2$ |
| HCl | 2775.6–2775.9<br>2925.7–2926.1 | – | $H_2O$, $CO_2$, $O_3$,<br>$N_2O$, $CH_4$, $NO_2$ |
| HF | 4038.8–4039.1 | surface +80 km | $O_3$, $CH_4$ |
| $N_2O$ | 2481.2–2482.5 | – | $H_2O$, $CO_2$, $O_3$,<br>$CH_4$ |
| $CH_4$ | 2835.5–2835.8<br>2903.6–2904.3 | – | $H_2O$, $O_3$, HCl |

the measurements more easily if compared to satellite experiments. Ground-based FTIR activities actually play an important role in the validation of satellite measurements.

Since March 1999 a Bruker 120M FTIR spectrometer has been operated routinely at the Izaña Observatory, yielding an unique 5-year time series of atmospheric trace gas profiles in a subtropical region. The measurements are performed as part of the Network for Detection of Stratospheric Change (NDSC). The NDSC, which is supported by the International Ozone Commission, the United Nations Environment Programme, and the World Meteorological Organization, is a network of observatories that provide long-term measurements of stratospheric parameters at high quality. In this paper time series of $O_3$, HCl, HF, $N_2O$ and $CH_4$ are presented. A detailed error analysis of the FTIR results is performed and the measurements are compared to 3-D model calculations.

## 2 The measurements

### 2.1 Measurement site

The Izaña Observatory is located on the Canary Island of Tenerife, 300 km from the African west coast at 28°18′ N, 16°29′ W at 2370 m a.s.l. Its position in the Atlantic Ocean and above a stable inversion layer, typical for subtropical regions, provides clean air and clear sky conditions for most of the year, offering excellent conditions for stratospheric observations by remote sensing techniques. The interseasonal variability of some geophysical parameters are given in Schneider (2002). In winter (December to April) the mean 2 PVU dynamical tropopause height is 10.5 km, although large variations are observed, i.e. both typical mid-latitudinal values of 8–10 km and typical tropical values of 13–16 km are possible. In summer (July to September), when there are less disturbances in the upper troposphere and stratosphere, the tropopause height is relatively stable and is located around 14.5 km. This pronounced interseasonal and day-to-day variability in winter is typical of a subtropical region since it is the transition area from the high tropical tropopause to the lower mid-latitude tropopause. The stratospheric zonal winds are geostrophic and therefore westerlies prevail from November to April and easterlies from May to October. Meridional flow in the stratosphere is driven by wave disturbances, which are more important in winter, when backward trajectories show that the origins of airmasses detected at Izaña are widely dispersed, i.e. both tropical and polar airmasses are detected on occasions. In summer stratospheric airmasses tend to originate from around 20–25° N with little variation.

### 2.2 Spectra evaluation

The solar absorption spectra are measured with a Bruker 120 M with a resolution of 0.0036–0.005 $cm^{-1}$ when no numerical apodization is applied. The solar radiation is captured by a solar tracker controlled by both astronomical calculations and a quadrant sensor. A KBr beam splitter is used. Depending on the spectral region to be analyzed, liquid-nitrogen-cooled HgCdTe and InSb detectors are used to determine the spectral intensities. Both detectors operate in a photovoltaic mode with negligible non-linearities. Between March–August 1999 and February–March 2000 a photoconductive HgCdTe detector was applied for the 700–1200 $cm^{-1}$ wavenumber region. Its non-linearities were corrected. The spectra are typically constructed by co-adding up to 8 scans recorded in about 10 or 13 min, depending on their resolution. Analyzing the shape of the absorption lines (lines are widened by pressure broadening) and their different temperature sensitivities allows the retrieval of the vertical distribution of the absorbers. Since the instrumental line shape (ILS) also affects the shape of the measured absorption lines, it is desirable to determine this instrumental characteristic independently from the atmospheric measurements. This is done every two months, on average, using cell measurements and the software LINEFIT, as described in Hase et al. (1999). The measured spectra are analyzed with the inversion code PROFFIT (Hase et al., 2004), which applies the Karlsruhe Optimized and Precise Radiative Transfer Algorithm (KOPRA, Höpfner et al., 1998; Kuntz et al., 1998; Stiller et al., 1998) as a radiative transfer model. Since there is too little information in the ground-based spectra to retrieve the vertical distribution of the absorbers unambiguously, additional constraints have to be applied during the analysis. The inversion is performed on logarithmic scale. This positivity constraint avoids negative mixing ratios. Furthermore all profiles are constrained towards the shape of their a-priori profiles. In some cases they are additionally forced towards the absolute a-priori values at surface and above 80 km. The analyzed microwindows, the additional constraints, and the interfering gases are listed in Table 1. A-priori data are HALOE climatological profiles for HF and $CH_4$, climatological profile of Tenerife's ozone sondes for $O_3$, and climatologies of mid-latitudes shifted by 3 km in height for HCl and $N_2O$. Up to 30 km temperature data are taken from the meteorological

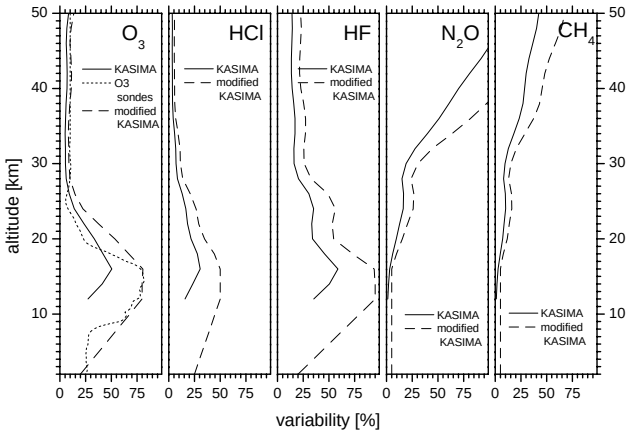


**Fig. 1.** Variability of trace gas profiles (%) calculated directly from the KASIMA 3-D CTM (solid line) and scaled by a factor 1.6 (dashed line). The $O_3$ panel also shows the variability determined from sonde measurements.

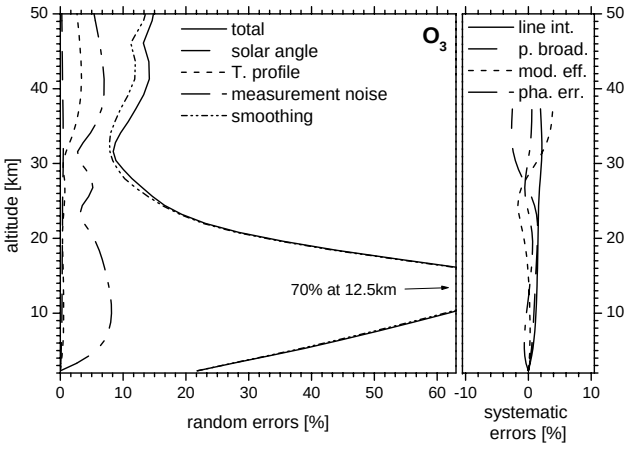


**Fig. 2.** Estimated errors (%) of $O_3$ profiles for random errors (left) and systematic errors (right). The lines are described in the text.

soundings performed each day at 12:00 UT and above those supplied by the automailer system of the Goddard Space Flight Center are used.

### 2.3 Error analysis

The error analysis is based on the work of Rodgers (2000), according to which the error in the retrieved profiles separates into three components; errors due to uncertainties in the input parameters applied in the inversion procedure, errors due to measurement noise, and errors due to the inherent finite vertical resolution of the observing system, subsequently called the "smoothing error". The confidence of this method for the error estimation for $O_3$ was demonstrated in Schneider et al. (2005). There it was also shown that the retrieved $O_3$ profile are consistent with ECC-sonde and HALOE (Halogen Occultation Experiment) data.

#### 2.3.1 Error analysis: model input parameters

Input parameters are solar elevation angle, temperature profile, ILS, and spectroscopic line parameters. Discrepancies between the angle under which the solar radiation enters the instrument and the actual solar elevation angle, which is applied in the retrieval, may occur when the instrument's aperture is not centred on the solar disk. For the error estimations an uncertainty of 0.1° was assumed (the diameter of the solar disc is 0.5°). Temperature uncertainties of 2.5 K near the surface and 14 K in the upper stratosphere are assumed. They arise from the limited accuracy of the sonde's thermometer and mismatches in time and space for the airmasses detected by FTIR and sonde. The modulation efficiency and the phase error are assumed to be determined by the cell measurements at an accuracy of 2% and 0.2 rad, respectively. Spectroscopic line parameters are generally taken from the HITRAN 2000 database (Rothman et al., 2003) with an assumed accuracy of 5%. For $O_3$ data are taken from Wagner et al. (2002), who estimate an accuracy of 2% for line intensity and pressure broadening coefficient.

#### 2.3.2 Error analysis: measurement noise

Noise in the measured spectrum has an important impact on the quality of the measurement. Around 785 $cm^{-1}$, where $O_3$ is evaluated the signal-to-noise ratio is typically 250. At 2482 $cm^{-1}$ ($N_2O$) it is 490, around 2800 $cm^{-1}$ (HCl and $CH_4$) it is 470–660, and at 4039 $cm^{-1}$ (HF) it is 800.

#### 2.3.3 Error analysis: smoothing

The application of constraints limits the vertical resolution of the retrieved profiles, which gives rise to an important error – the so-called smoothing error. For a statistical analysis of this error, which is given by the difference between the retrieved smoothed profile and the real atmospheric profile, the variability of the real profile and its covariance must be known. For $O_3$ this information can be obtained from the weekly ozone soundings, which shows large variability in the tropopause region (up to 80%) and a correlation length of typically 2.5 km. The natural variability of the other gases is estimated from the annual variabilities calculated by the KASIMA 3-D CTM. These modelled variabilities are very likely to differ from the real variabilities due to deficiencies of the model, e.g. limited vertical and horizontal resolution. A comparison of the $O_3$ variabilities obtained from the sondes and KASIMA (dotted and solid line in left panel of Fig. 1) shows that the real variability exceeds the modelled one by approximately 60% above 16 km. Hence, for the estimation of the smoothing error of HCl, HF, $N_2O$, and $CH_4$, a modified KASIMA variability (original KASIMA variability multiplied by 1.6, see Fig. 1) is applied. The interlevel correlations for all gases are assumed to be those of the $O_3$

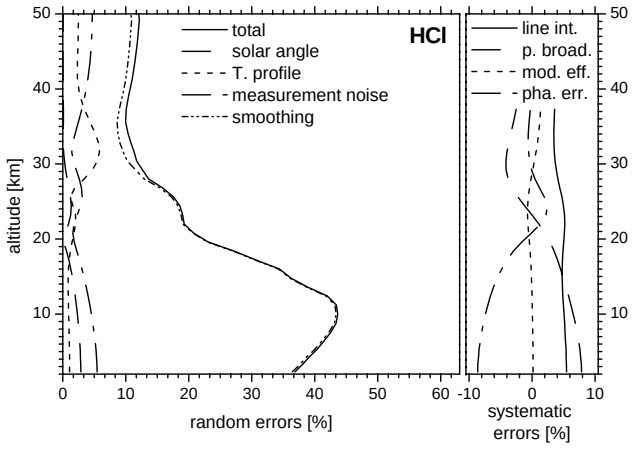


**Fig. 3.** As Fig. 2 but for HCl profiles.

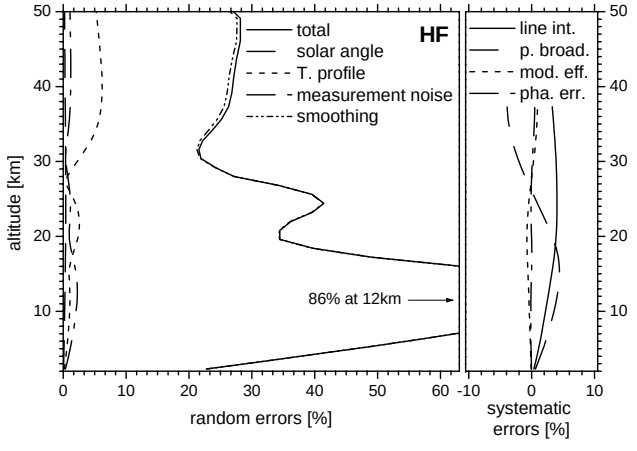


**Fig. 4.** As Fig. 2 but for HF profiles.

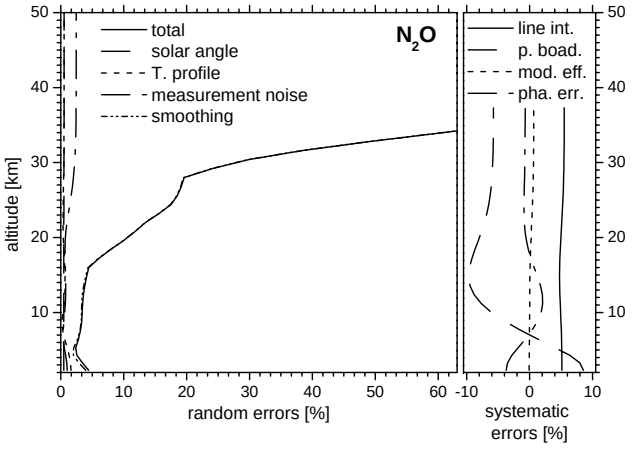


**Fig. 5.** As Fig. 2 but for $N_2O$ profiles.

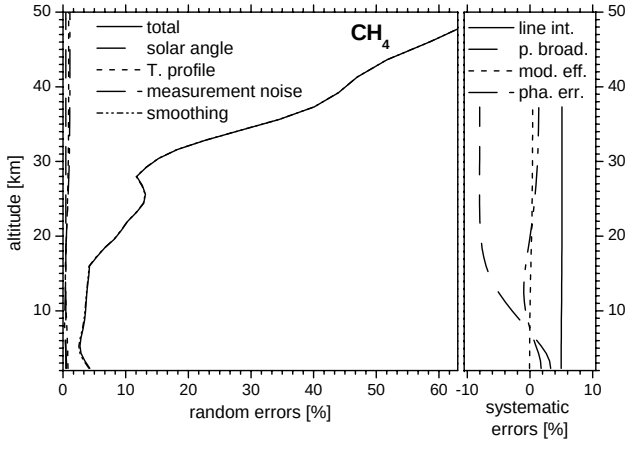


**Fig. 6.** As Fig. 2 but for $CH_4$ profiles.

sondes, i.e. Gaussian-like with correlation length of 2.5 km throughout the atmosphere.

#### 2.3.4 Error analysis: summary

Errors due to solar angle, temperature profile, measurement noise, and smoothing are random. As shown in Figs. 2 to 6 the smoothing error is by far the most important source of uncertainty in the retrieved profile, followed by the measurement noise and temperature profile errors. Errors caused by uncertainties in the solar angle can generally be neglected. It should be noted that the variabilities, temperature profile, measurement noise and smoothing error, as depicted in Figs. 1 to 6, do not reflect all interlevel correlations. A proper presentation would only be possible in form of the so-called error patterns (Rodgers, 2000). For a single profile, uncertainties in the ILS and line parameters are responsible for systematic errors. Below ∼20 km for the tropospheric source gases $N_2O$ and $CH_4$ the systematic line parameter errors clearly exceed the estimated precision. The estimated random and systematic errors in the total, tropospheric, and stratospheric column amounts are presented in Table 2. This confirms that the uncertainties in the line parameters dominate the error for tropospheric gases and that the smoothing error and measurement noise determine the precision of the tropospheric column amounts of stratospheric gases.

### 2.4 Characterization of retrieved profiles

Instead of estimating the quality of the retrieved profile by quoting the large smoothing errors it may be useful to consider just the smoothed profiles and analyze a-priori what kind of features of the real atmosphere are expected to be observable in the retrieved profiles. The averaging kernels are commonly used for this purpose as they give an impression of the vertical resolution of the retrieved profiles.

Figure 7 shows the averaging kernels for the retrieved mixing ratios. Their amplitudes indicate the sensitivity of the retrieval and their full widths at half maximum (FWHM) indicate the vertical resolution of the corresponding layer. In the

**Table 2.** Estimated errors of total, tropospheric, and stratospheric column amounts (tropospheric/stratospheric values are for below/above 12.4 km; in parenthesis).

| Error source | $O_3$ [%] | HCl [%] | HF [%] | $N_2O$ [%] | $CH_4$ [%] |
|---|---|---|---|---|---|
| solar angle | 0.7 (0.5/0.8) | 0.7 (1.4/0.7) | 0.6 (0.3/0.6) | 0.5 (0.5/0.4) | 0.8 (0.9/0.8) |
| T. profile | 0.7 (1.6/0.8) | 1.0 (2.0/1.0) | 1.6 (1.3/1.6) | 0.4 (0.7/0.5) | 0.5 (0.6/0.5) |
| meas. noise | 1.2 (7.1/1.0) | 1.2 (12.9/0.7) | 0.6 (4.0/0.6) | 0.2 (0.3/0.5) | 0.3 (0.4/0.6) |
| smoothing | 1.5 (26.7/1.9) | 1.1 (32.7/1.3) | 1.8 (72.6/1.7) | 0.3 (0.5/1.4) | 0.2 (0.5/1.3) |
| **total random** | **2.6 (28.0/2.8)** | **2.2 (35.8/2.0)** | **2.7 (72.8/2.6)** | **0.8 (1.1/1.7)** | **1.2 (1.5/1.9)** |
| line int. | 1.8 (0.8/1.9) | 4.3 (9.8/4.5) | 4.3 (2.3/4.4) | 5.1 (5.3/4.6) | 5.0 (5.0/5.0) |
| pres. coef. | 0.1 (0.7/0.1) | 0.6 (13.1/0.8) | 0.3 (3.3/0.2) | 0.9 (1.4/8.7) | 1.0 (0.8/7.2) |
| mod. eff. | 0.1 (0.2/0.1) | 0.1 (0.4/0.1) | 0.0 (0.5/0.1) | 0.0 (0.0/0.1) | 0.0 (0.0/0.2) |
| pha. err. | 0.2 (0.8/0.2) | 0.6 (6.2/0.3) | 0.6 (0.7/0.6) | 0.2 (0.3/0.3) | 0.3 (0.5/0.5) |

**Table 3.** Typical vertical resolution of FTIR profiles at some selected altitudes.

| Alt. [km] | $O_3$ [km] | HCl [km] | HF [km] | $N_2O$ [km] | $CH_4$ [km] |
|---|---|---|---|---|---|
| 2.3 | 13.5[a] | – | 14.8[a] | 9.1[b] | 11.1[b] |
| 10.0 | 14.7[a] | – | 15.4[a] | 11.7 | 15.4 |
| 14.8 | 15.6 | – | 16.5 | 12.3 | 21.7[a] |
| 17.2 | 15.8 | 15.7[a] | 17.4 | 16.8 | – |
| 22.0 | 14.6 | 15.9 | 18.8[a] | – | – |
| 24.4 | 12.3 | 13.6 | 22.0[a] | – | – |
| 26.8 | 11.4 | 17.7 | 32.9 | – | – |
| 28.0 | 13.0 | 21.7[a] | 34.2[a] | – | – |
| 29.2 | 17.0 | 20.6[a] | 33.6[a] | – | – |
| 30.4 | 21.2 | – | 33.2 | – | – |
| 31.6 | 24.0[a] | – | 32.9[a] | – | – |
| 39.2 | 25.1 | – | 32.4[a] | – | – |

[a] peak does in general not coincide with nominal altitude
[b] half sided FWHM

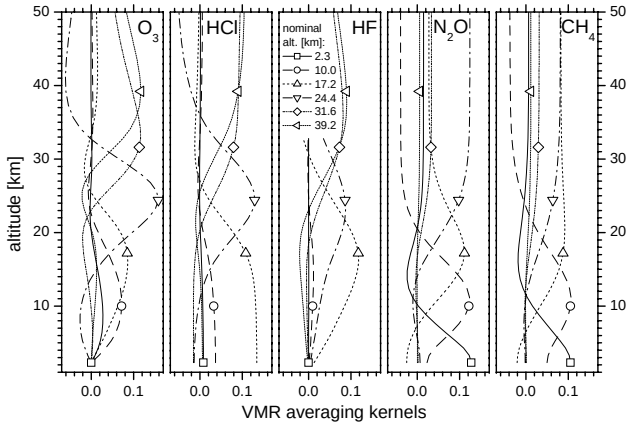


**Fig. 7.** VMR averaging kernels.

case of Tenerife Island, they are particularly small for solar elevation angles around or below 20°. Typical FWHM values are listed in Table 3. At altitudes close to the surface the FWHM is calculated as double the distance between the altitude of the kernel's maximum and the altitude above, where it reaches its half value. For $O_3$, HCl, and HF below ∼20 km and above 32 km the kernels' maxima do not coincide with the nominal height, which makes it more difficult to interpret the FWHM. The best vertical resolution is achieved by $O_3$ around 26 km with FWHM values between 9.0 and 12.5 km. HCl and HF have smallest FWHMs of around 13 km at 24 km and of 18 km at ∼18 km, respectively. $N_2O$ and $CH_4$ are well suited for an analysis of the atmosphere below 20 km with typical FWHMs as small as 9.1 km.

The trace of the averaging kernel matrix provides another useful measure. It gives the number of independent pieces of information retrieved from the measurement. For the $O_3$ retrievals the trace of the averaging kernel matrix is around 3.0 and for the HCl retrievals around 2.7, indicating the possibility of retrieving up to 3 independent components in the profile, whereas the trace of the HF kernels is typically around 2.1. The spectra used for the $N_2O$ and $CH_4$ retrievals contain 3.0 and 2.4 independent pieces of information.

The capability of the retrieved profile to describe the real profile can be even better assessed by using some a-priori information. The kernels of Fig. 7 are the response of the retrieved profiles on altering the mixing ratio at the nominal height of the real profile by 1 arbitrary unit. If one tries to estimate which altitude range of the real atmosphere is typically represented in the mixing ratio retrieved at a certain altitude level, it is necessary to consider not only the averaging kernels but also the typical variability and the interlevel correlations in the real atmosphere. This information, in form of a covariance matrix $\mathbf{S_a}$, is obtained from a statistical analysis of KASIMA calculations and $O_3$ sondes as described in Sect. 2.3.3. An eigenvector analysis of the matrix $\mathbf{S_a}$ allows

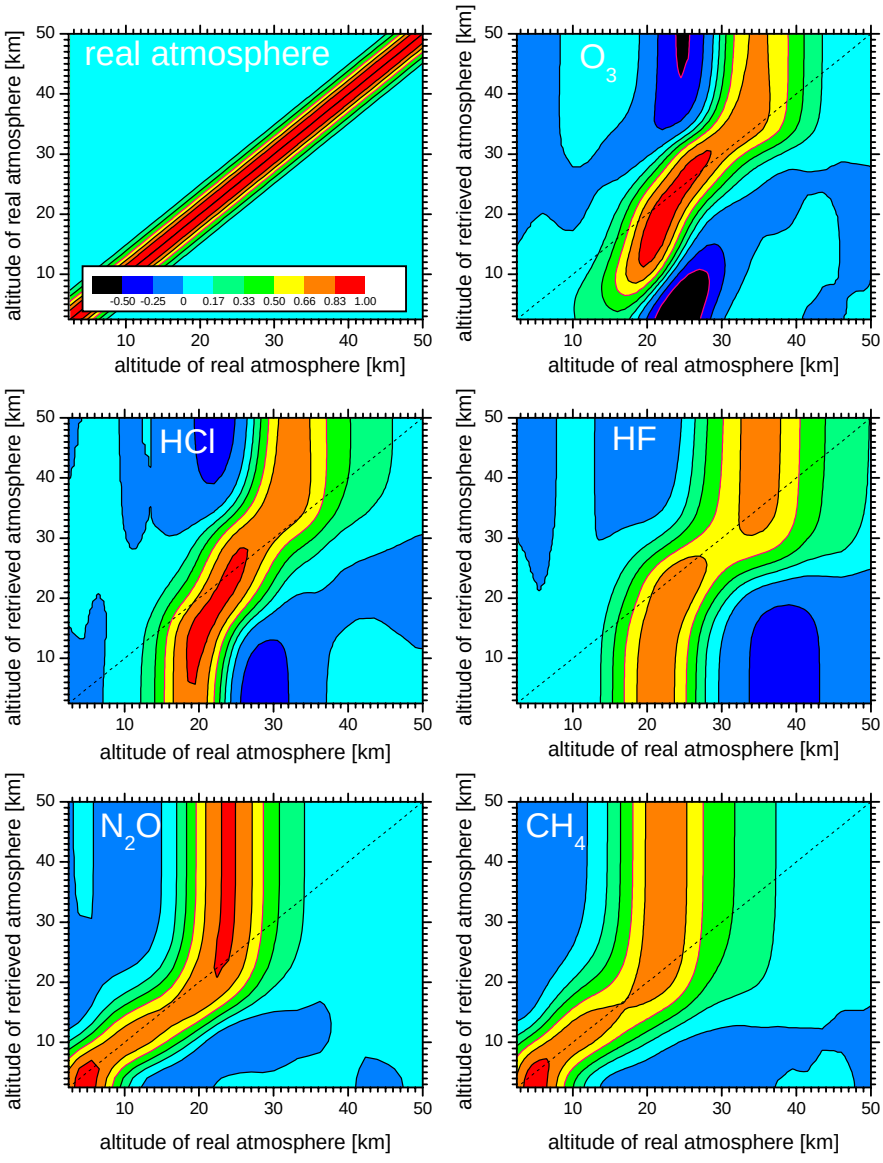


**Fig. 8.** Sensitivity analysis of the retrieved profiles (for more details see text). Upper left panel: interlevel correlations in the real atmosphere; all other panels: correlations between real atmosphere and retrieved atmosphere. The line for a coefficient of 0.5 or −0.5 is depicted in pink.

us to identify the components of the real profile, which vary independently from each other. They are represented by the eigenvectors of $\mathbf{S_a}$ multiplied by their respective eigenvalues. These scaled vectors contain the same information as the covariance matrix. Any possible variation of the real profile can be represented by a linear combination of these vectors, whereby their coefficients are randomly distributed with a mean of 0 and a variance of 1. Multiplying a simulated real profile with the averaging kernel yields its corresponding retrieved profile. An ensemble of a large number of simulated real profiles and their corresponding retrieved profiles represents the variability and interlevel correlations of the real and their corresponding retrieved profile. Correlating the real to their corresponding retrieved profiles allows us then to identify the altitude ranges in the real profile which are, from a statistical point of view, mainly represented at a certain altitude level of the retrieved profile.

The results of this sensitivity analysis are shown in Fig. 8 for the typical kernels depicted in Fig. 7. The upper left panel shows the interlevel correlations in the real atmosphere, i.e. the sensitivity for an optimal retrieval. The assumed Gaussian-like interlevel correlation with a $\sigma$ value of 2.5 km produces correlation coefficients of at least 0.5 (in the following called $0.5\rho$-layer) within a layer of 3.5 km around the nominal altitude. The limits of this layer are marked by a pink line. The correlation coefficients of a real retrieval

are smaller and their $0.5\rho$-layers are broader, since they are influenced by the a-priori profiles. $O_3$ shows largest coefficients of 0.94 for a correlation between the real mixing ratio at 22 km and the retrieved mixing ratio at 20 km, i.e. the $O_3$ is especially sensitive to the real atmospheric $O_3$ amounts around 22 km. The retrieved value at 32 km correlates with the real value at 30 km with 0.8. At 20 and 32 km the $0.5\rho$-layers ranges from 18 to 25 km and from 26 to 36 km, respectively. The ratios retrieved above 40 km and below 10 km show strong anti-correlations to the real values around 25 km, which complicates the interpretation of the retrieved values at these altitudes. The HCl retrieval is most sensitive to altitudes around 20 km, which correlate to the mixing ratio retrieved at 16 km with a coefficient of 0.89. At altitudes below 13 km the $0.5\rho$-layer covers the real profiles between 15 and 23 km. The values retrieved above 30 km have correlation coefficients below 0.8 and above 40 km the $0.5\rho$-layer is situated between 28 and 37 km. The retrieved HF is less sensitive to the real atmosphere. It shows largest coefficients of 0.82 at 22 km for correlation with the real mixing ratio at 24 km. Its $0.5\rho$-layer covers 8–10 km. $N_2O$ and $CH_4$ are well suited for analyzing the atmosphere below 25 km, where their maximal correlations correspond to the nominal altitudes. The coefficients reach 0.9 for altitudes below 5 km and 0.85 at 23 km (for $N_2O$). The latter makes the $N_2O$ retrieval appropriate for an analysis of the lower stratosphere.

## 3 The models

### 3.1 SLIMCAT

The SLIMCAT three-dimensional (3-D) off-line chemical transport model (CTM) is described in detail by Chipperfield (1999). The model temperatures and horizontal winds are specified from analyses and the vertical transport in the stratosphere is diagnosed from radiative heating rates. In the stratosphere the model uses an isentropic coordinate and this has been extended down to the surface using hybrid sigma-theta levels. The troposphere is assumed to be well-mixed. The model has a detailed treatment of stratospheric chemistry including gas-phase and heterogeneous chemistry.

In the run used here SLIMCAT was integrated with a horizontal resolution of $7.5^\circ \times 7.5^\circ$ and 20 levels extending from the surface to about 55 km. The model was forced by European Centre for Medium Range Weather Forecasts (ECMWF) analyses and the simulation started 1 January 1989. ERA-40 analyses were used until 31 December 1999 followed by operational analyses. The model source gas loadings were from tropospheric observations (WMO, 2003). The output was saved at 00:00 UT every 2 days interpolated to the location of Izaña.

### 3.2 KASIMA

The KASIMA (Karlsruhe Simulation model of the Middle Atmosphere) 3-D CTM has a unique model architecture as it couples a mechanistic model with an off-line model which is forced by meteorological analyses (Kouker et al., 1999). The model run used here was initialized on 15 October 2000 with zonal mean output from the REPROBUS 3-D CTM (Lefevre, personal communication). Tropospheric trends of the source gases as $N_2O$, $CH_4$, and the CFCs were prescribed during the model run (Engel, personal communication). The meteorology is based on operational ECMWF analyses up to 1 hPa and the mechanistic model on top. The horizontal resolution was approximately $4.0^\circ \times 4.0^\circ$ (T30). The run used 63 vertical levels between 10 and 120 km pressure altitude with a 0.75 km spacing from 10 up to 22 km and an exponentially decreasing resolution above. For the comparison with the FTIR data model output for 12:00 UT each day during the simulation was used.

KASIMA therefore provides a slightly higher resolution view of the stratosphere but for a shorter period. In contrast, the multi-decadal run of SLIMCAT ensures that all of the model long-lived tracers have "spun-up" and are independent of any initialisation.

## 4 Observed time series

### 4.1 Results of the measurements

The open circles in the upper panels of Figs. 9 to 13 represent the time series of the FTIR-observed stratospheric column amounts (above 12.4 km altitude) of the trace gases from March 1999 until December 2003. HF, which is chemically long-lived and more abundant at higher altitudes, and $N_2O$, which is long-lived and abundant at lower altitudes, show annual cycles with gradually decreasing (HF) and increasing ($N_2O$) column amounts and low variability during summer. In winter large column amounts of HF, small column amounts of $N_2O$ and large variabilities are observed. These observations reflect the pronounced upwelling and stable stratosphere in summer and the more disturbed stratosphere in winter. The time series of the profiles, which are depicted in the second panels from the top of Figs. 9 to 13 show, that the mixing ratio isolines typical for the lower stratosphere, e.g. the 0.3 ppbv HF isoline or 0.3 ppmv $N_2O$ isoline ascend gradually and stably during summer and are situated at low altitudes and show strong variabilities in winter. For the chemically active trace gas $O_3$ this dynamical evolution of the atmosphere is also observed, e.g. the 1.5 ppmv $O_3$ isoline, ascends gradually during summer and shows relatively strong variabilities in winter. However, for $O_3$ the photochemistry is also important. In summer when solar irradiation is very intensive at Izaña (solar elevation of 85.2° at summer solstice) the ozone production above 25 km

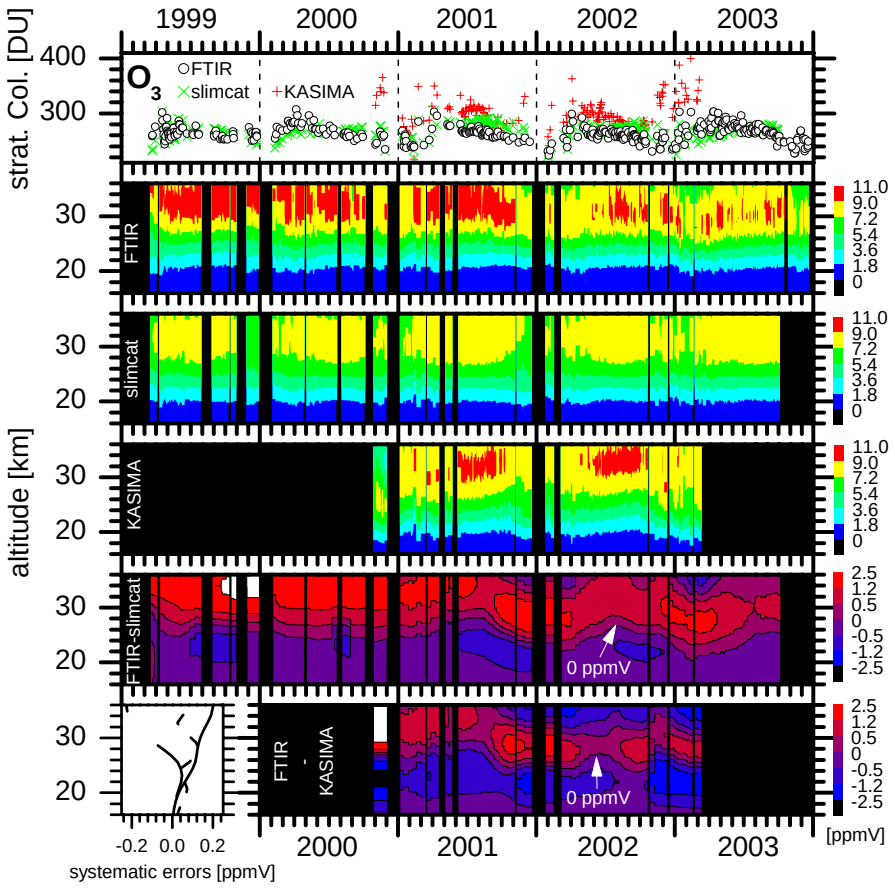


**Fig. 9.** $O_3$ time series. Upper panel shows stratospheric column amounts (above 12.4 km). Black circles: FTIR; green crosses: SLIMCAT; red crosses: KASIMA. Second to fourth panel depict mixing ratio profiles of FTIR, SLIMCAT and KASIMA (with the vertical resolution of FTIR), respectively. Two lower panels show the difference between FTIR and SLIMCAT and FTIR and KASIMA profiles for timescales greater than 2 months. Left hand side of lower panel depicts the systematic errors for the difference of FTIR and models. Solid line: line intensity (+2%); dashed line: pressure broadening coefficient (+2%); dotted line: covariance smoothing error.

is enhanced, which dampens the cycle observed in the column amount series of $O_3$ compared to the purely dynamical cycles of HF and $N_2O$. This photochemical cycle is tracked by the FTIR profile series which show $O_3$ mixing ratios of typically 8.5 ppmv around 32 km in winter and of 10.0 ppmv in summer.

The behaviour of HCl is also mainly dominated by the above-mentioned dynamical processes as can be observed in the evolution of its profile series. However since it is chemically less stable than HF other processes have also to be considered, e.g. its chemical destruction by reaction with OH, which is more abundant in the summer stratosphere than in the winter stratosphere. $CH_4$ shows similar temporal evolution as $N_2O$, however it is correlated to the chemical chlorine partitioning by its reaction with Cl to $CH_3$ and HCl, which accounts for approximately 30% of the total destruction of $CH_4$ in the stratosphere (Lary and Toumi, 1997).

## 4.2 Measurements versus models

The vertical resolution of the modelled and measured profiles are different, which has to be considered for an adequate comparison. The averaging kernels of the FTIR profiles have FWHMs of 10–20 km. The model calculations are on a far finer grid and their vertical resolutions are up to 0.75 km in the lower stratosphere and about 2 km in the upper stratosphere. Hence, compared to the FTIR observations the modelled profiles are highly resolved. They have been transformed to the FTIR resolution by smoothing with the FTIR averaging kernels. Since KASIMA only calculates mixing ratios between 12 km and 70 km and SLIMCAT only up to 60 km the a-priori data were applied to complete the modelled profiles over the whole altitude range covered by the averaging kernels. This procedure excludes influences of the altitudes where no model data exist on other altitude levels. The third and fourth panels of Figs. 9 to 13 show the time series of the smoothed model profiles. In general

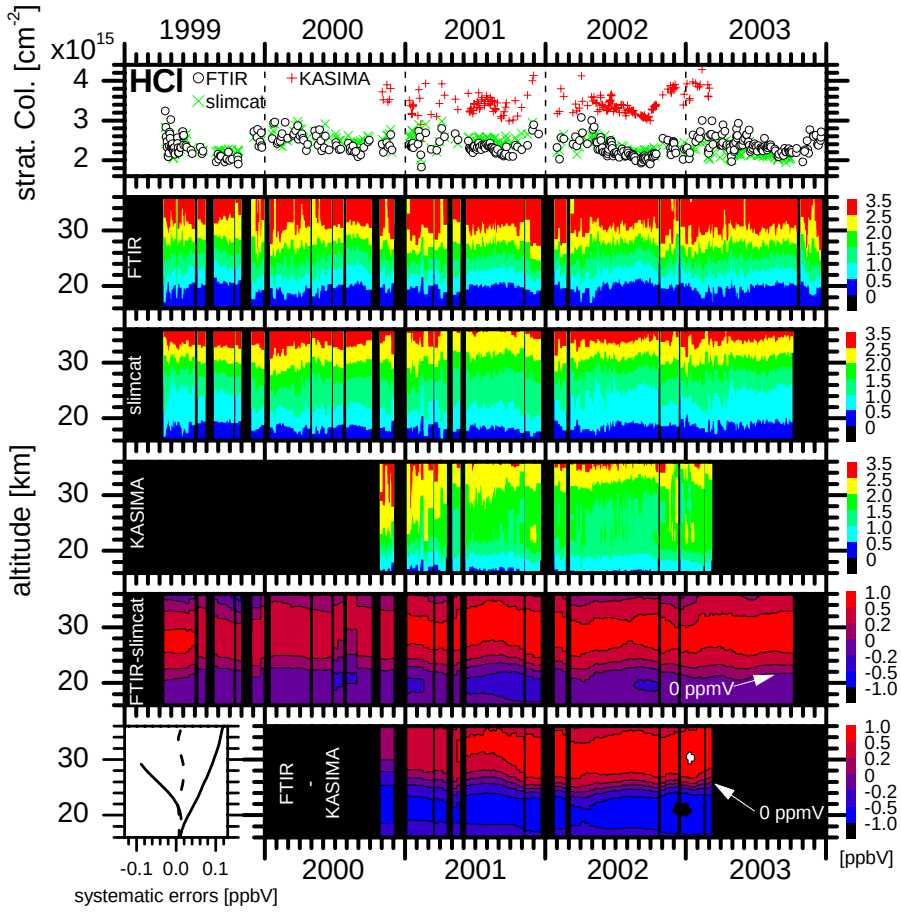


**Fig. 10.** Same as Fig. 9 but for HCl and an assumed uncertainty of +5% for line intensity and pressure broadening coefficient (left hand side of lower panel).

the models calculate the same annual cycles as observed in the measurements, i.e. upward shifted profiles around the tropopause/lower stratosphere region during summer and higher variability in winter than in summer. The enhanced photochemistry observed by an especially pronounced ozone maximum in summer is also well documented by KASIMA, while SLIMCAT differs in this respect. Abrupt changes in the profiles, which occur suddenly when tropical or polar airmasses are detected, are generally tracked by the models in agreement with the measurements. From 6–10 February 2001 a tropical streamer event was detected over Izaña (on those days tropical airmasses were present; Schneider, 2002), which caused an upward shift of the profiles in the lower stratosphere of about 4 km. This can be seen particularly well in the chemically stable gases HF and $N_2O$. Simultaneously, the $O_3$ mixing ratios above 25 km increase during this event, which is observed in the measured as well as in the simulated KASIMA profiles, but not in the SLIMCAT profiles, which have a lower resolution. Similarly, the downward shift of the HF and $N_2O$ profiles observed from 10–13 February 2003 is due to the presence of polar airmasses.

However, there are important differences between measurement and models. The time series of the differences between FTIR and model profiles are shown in the two lower panels of Figs. 9 to 13. These have been additionally smoothed along the temporal scale by a 2-month running mean, which consists in averaging all data available between 1 month before and 1 month after the day of reference. This procedure makes the temporal evolution during the modelled period clearer, however, the running mean so-obtained is less confident for periods where less measurements are made. For an adequate interpretation of these differences the systematic errors coming from the FTIR profiles have to be estimated. Similar to Eq. (11) in Schneider et al. (2005), the expected uncertainty for the difference between the FTIR and smoothed model profiles can be calculated from:

$$\begin{aligned} \boldsymbol{x}_{err} &= \mathbf{AI}_{][}(\boldsymbol{x}_{real} - \boldsymbol{x}_{a-priori}) \\ &+ \mathbf{GK_p}\boldsymbol{\epsilon}_p + \mathbf{G}\boldsymbol{\epsilon}_y \\ &+ \mathbf{AI}_{[]}\boldsymbol{\epsilon}_{model}. \end{aligned} \quad (1)$$

Here $\boldsymbol{x}_{err}$, $\boldsymbol{x}_{real}$, and $\boldsymbol{x}_{a-priori}$ are the state vectors of the error, the real, and the a-priori profile, respectively. **A** is the

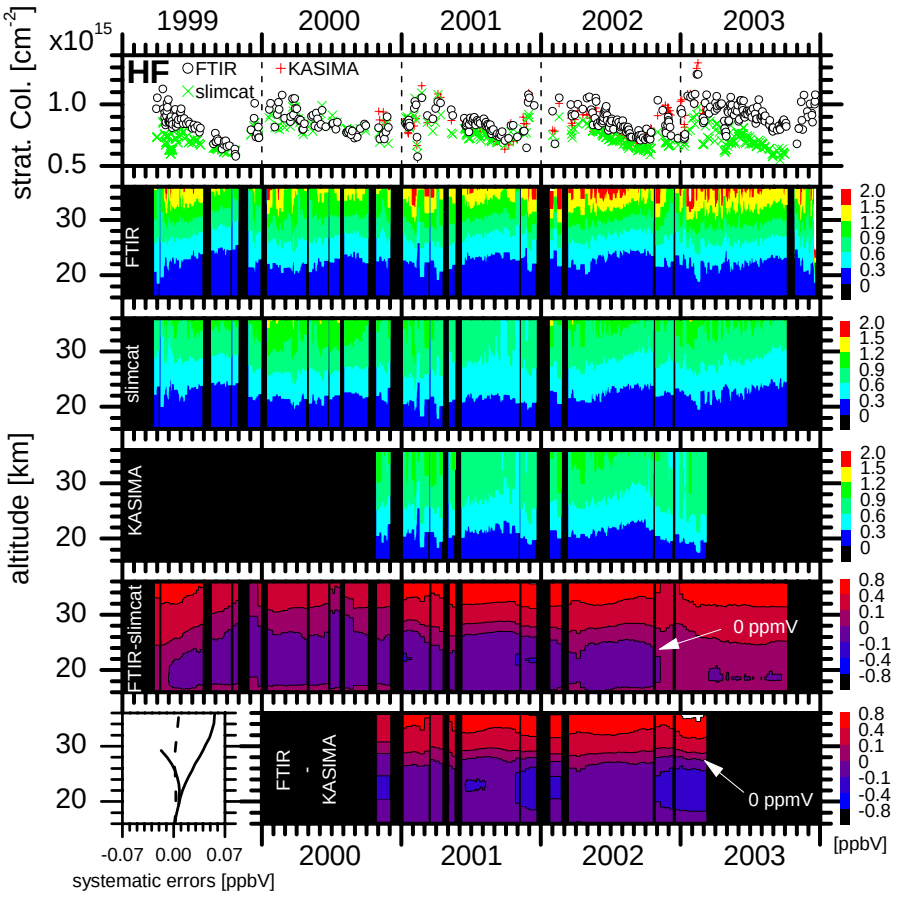


**Fig. 11.** Same as Fig. 9 but for HF and an assumed uncertainty of +5% for line intensity and pressure broadening coefficient (left hand side of lower panel).

FTIR averaging kernel matrix, $\mathbf{I}$, $\mathbf{I}_{[]}$, and $\mathbf{I}_{][}$ are unity matrices with entries at all levels, at levels corresponding to the altitude range of the model, and at levels covered by the FTIR inversion algorithm but not by the model. $\mathbf{G}$ is the gain matrix, $\mathbf{K_p}$ the sensitivity matrix for the model parameters and $\boldsymbol{\epsilon_p}$, $\boldsymbol{\epsilon_y}$, and $\boldsymbol{\epsilon_{model}}$, the retrieval model parameter, measurement and model uncertainties. In Eq. (1) the first term accounts for the smoothing error. Within the model's altitude range smoothing errors of FTIR and model are fully correlated and hence eliminate each other. Outside the model's altitude range the model profiles are extended with the constant a-priori data, which is left unchanged by smoothing. Hence, all smoothing errors present in the difference of FTIR and model profiles are produced by smoothing the FTIR profile at these altitude ranges. Concerning an ensemble of real atmospheric profiles from a whole annual cycle, the smoothing error is a pure random error with the real profiles varying randomly around the a-priori profile, since it is an all-season climatology. However, in the following seasonal variabilities of the difference between FTIR and model profiles are discussed, and an ensemble of profiles sampled on smaller timescales may have systematic smoothing errors, since its mean is different from the a-priori or all season climatology. This systematic smoothing error, like the smoothing error of a single FTIR profile in Sect. 2.3.3, is estimated by the covariances of the all season ensembles ($\mathbf{A}\mathbf{I}_{][}\mathbf{S_a}\mathbf{I}_{][}^{\mathbf{T}}\mathbf{A}^{\mathbf{T}}$). The second and third term of Eq. (1) contains the errors caused by uncertainties in the input parameters and FTIR measurement noise, of which only spectroscopic data may produce systematic errors. At the left hand side of the bottom of Figs. 9 to 13 the expected systematic errors for the difference between FTIR and smoothed model profiles are shown. The errors due to line parameter data are naturally independent from the model, whereas the systematic smoothing error depends on the model's altitude range. It is only shown for the difference between FTIR and KASIMA, since for SLIMCAT, which calculates at all altitude levels below 60 km, it can be neglected. These estimated errors are generally smaller than the observed differences, which allows us to attribute them to systematic errors of the model, which are represented by the last term in Eq. (1).

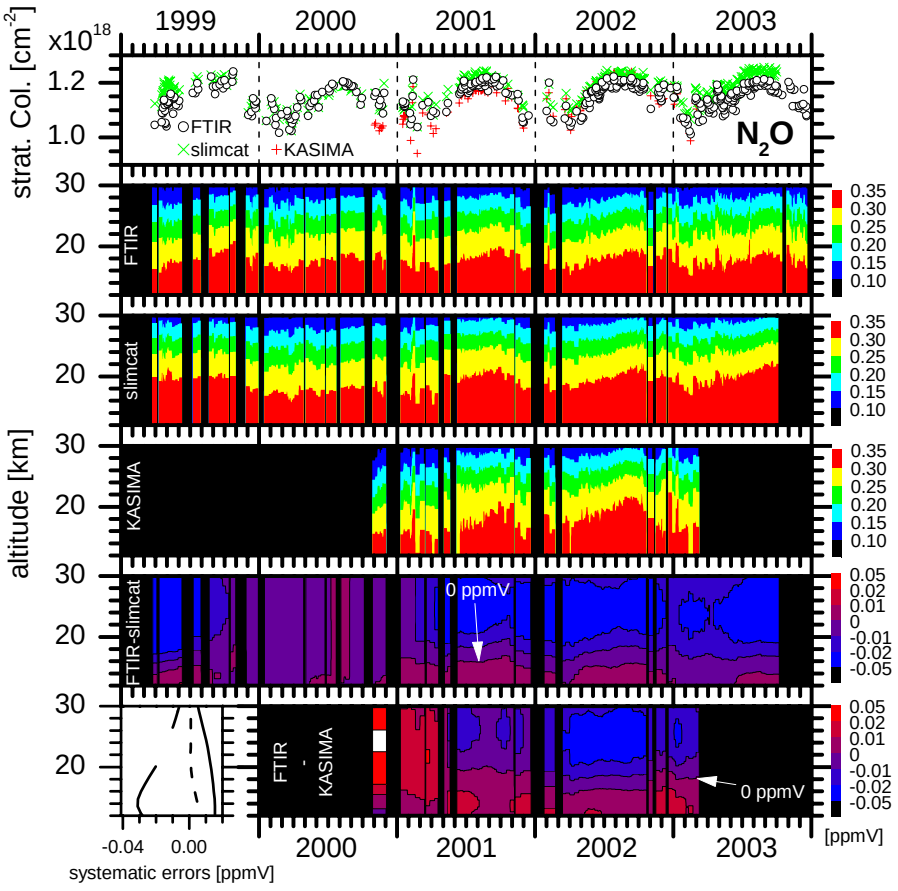


**Fig. 12.** Same as Fig. 9 but for $N_2O$ and an assumed uncertainty of +5% for line intensity and pressure broadening coefficient (left hand side of lower panel).

It is helpful to consider first the significant differences between models and measurements for the chemically relatively stable species HF, $N_2O$ and $CH_4$. As can be seen in the lower panels of Fig. 11 both models, if compared to the measurements, calculate smaller HF mixing ratios for higher altitudes. Hence, according to Fig. 8, the models underestimate the HF amounts above 30 km. The mixing ratios modelled for altitudes below ∼26 km are larger than their measured counterparts. This is most likely caused by the negative correlation at this retrieved altitude towards the real atmosphere above 30 km, where HF is underestimated by the models. For $N_2O$ (Fig. 12), on the other hand, the models overestimate the mixing ratios above ∼22 km and underestimate it below 20 km. The $N_2O$ mixing ratios retrieved at 22 km represent the real atmosphere quite well. It is impossible that these overestimations are produced artificially by too low model ratios at lower altitudes, since the anti-correlations towards mixing ratios below 15 km as observed in Fig. 8 are very small ($\rho$ values between −0.1 and −0.05). For $CH_4$ (Fig. 13) the same observations, even more pronounced, as for $N_2O$ are made. All the observed differences increase with time; faster for KASIMA than for SLIMCAT. HF exists only in very small amounts below the tropopause. It is produced in the stratosphere by photodissociation of CFCs, whereas $N_2O$ and $CH_4$ are emitted in the lower troposphere and oxidized in the stratosphere. Hence, too low model HF, too large model $N_2O$ and $CH_4$ and the observed trends, may indicate that the link to the tropical stratosphere, where upward transport is very effective, or the upward transport above Izaña itself is simulated too effectively.

Further similarities between the models are observed in the temporal evolution of their differences to the measurements. The models' under- or overestimations of stratospheric HF or $N_2O$ and $CH_4$, respectively, tend to increase in winter time (see lower panels of Figs. 11, 12, and 13). This means that during winter the differences between modelled and real dynamics tend to increase. On the other hand, at the end of spring and during summer the differences observed in the profiles decrease. This may indicate, that during this period the modelled and real atmospheric vertical motions are more consistent than in other periods.

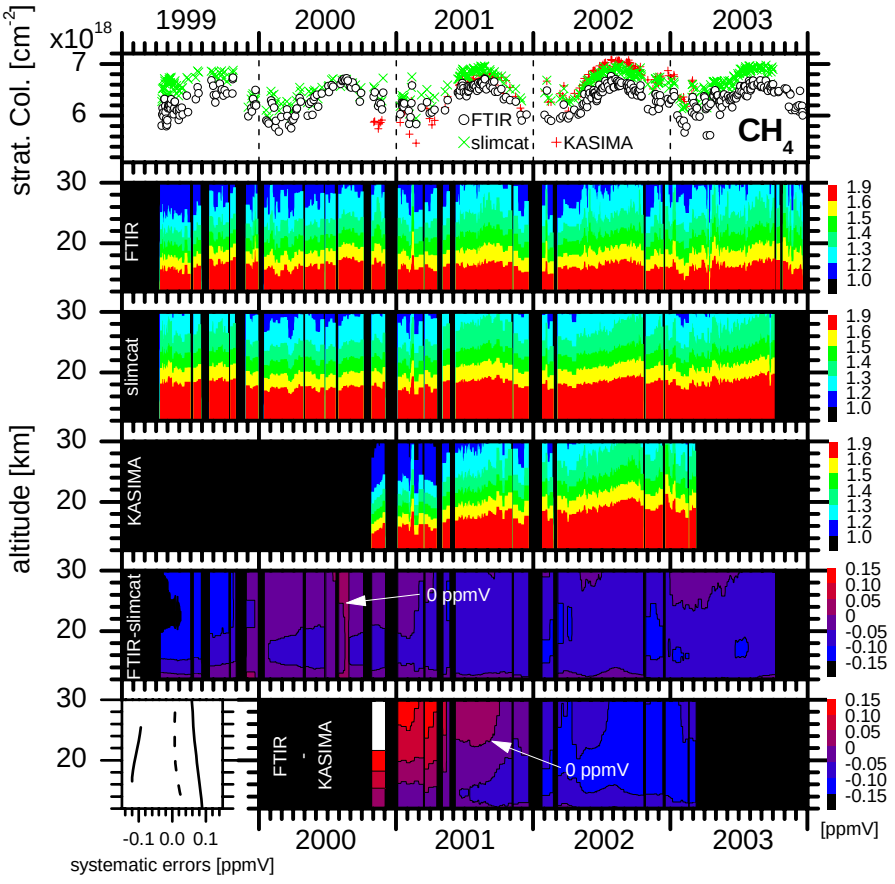


**Fig. 13.** Same as Fig. 9 but for $CH_4$ and an assumed uncertainty of +5% for line intensity and pressure broadening coefficient (left hand side of lower panel).

Interpretation of the chemically more active species $O_3$ and HCl is more complicated, since both dynamical and chemical processes and their interactions have to be considered. Both trace gases are, by analogy to HF, underestimated by the models, which is due to the mentioned dynamical deficiencies of the models. Too large model mixing ratios at low altitudes are, in particular for $O_3$, partly due to the anti-correlations with the underestimated values above in the middle stratosphere. However, at these altitudes the retrieved $O_3$ and HCl ratios also show large positive correlations with real atmospheric ratios at low altitudes (see Fig. 8). Hence, this overestimation cannot be explained only by an artefact introduced by the retrieval, but reflects most likely also the real atmospheric situation. Concerning $O_3$, the models (in particular SLIMCAT) clearly underestimate the increase in the $O_3$ mixing ratios in the middle stratosphere during summer. A similar enhanced difference at the end of summer, also less pronounced as for $O_3$, is observed for HCl. A reason might be a shorter lifetime of the precursor species (molecular oxygen and CFCs, respectively) and thus an enhanced production of $O_3$ and HCl (in-situ photochemistry) or a stronger link to their source region, the tropical stratosphere, in the real atmosphere (inner-extra tropical transport processes) if compared to the models. For both species, similar to the dynamical tracers, the differences show a periodic evolution. They decrease from winter to mid-summer and increase from mid-summer to winter. Hence the seasonal evolution of the difference between measurement and models precedes those of chemically stable species by approximately 3 months. These differences with respect to HF are due to the increasing underestimation of $O_3$ and HCl in the middle stratosphere in both models at the end of summer, which degrades the calculated model concentrations even more, since an incorrect simulation of middle stratospheric $O_3$ influences lower altitudes. A too thin $O_3$ layer causes an increase in the UV radiation at lower altitudes, and as a consequence an enhanced production of $O_3$ (photodissociation of molecular oxygen) and HCl (photodissociation of CFCs). Both can be observed in the lower panels of Figs. 9 and 10 at the end of summer. They are particularly pronounced for SLIMCAT, whose underestimation of middle stratospheric $O_3$ is more significant.

For 2000 and the beginning of 2001 the KASIMA profiles show strong trends since they are adjusting from somewhat inappropriate initializations to their state of model

**Table 4.** Sensitivity ranges of mixing ratios retrieved at some selected altitudes. Determined by the method described in Sect. 2.4.

| Species | Retrieved at [km] | 0.5$\rho$-layer [km] | Major contribution from [km] ($\rho$ value) |
|---|---|---|---|
| $O_3$ | 19.6 | 18–25 | 22 (0.94) |
| | 28.0 | 22.5–31 | 26.5 (0.88) |
| | 37.3[a] | 30–39 | 33.5(0.75) |
| HCl | 16.0 | 16–25 | 20 (0.89) |
| | 28.0 | 22–31 | 25.5 (0.84) |
| | 35.6 | 27–36.5 | 31 (0.80) |
| HF | 22.0 | 19–29 | 24 (0.82) |
| | 34.1 | 29–40 | 34.5 (0.71) |
| $N_2O$ | 22.0 | 18–27 | 22 (0.85) |
| $CH_4$ | 22.0 | 16.5–26.5 | 21.5 (0.76) |

[a] also anti-correlated to real mixing ratios around 25 km

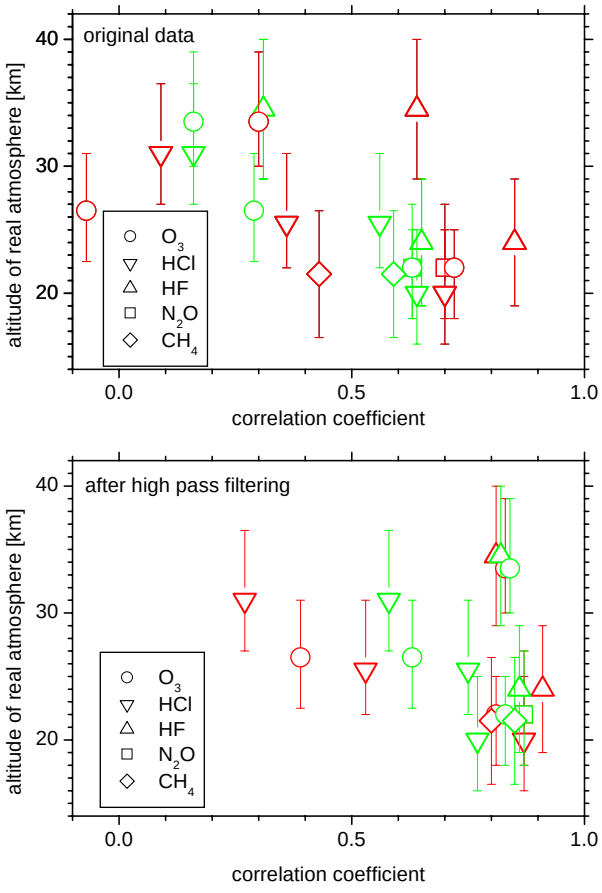


**Fig. 14.** Correlation coefficients between measured and modelled mixing ratios versus real atmospheric altitude. Upper panel depicts correlation for original data, lower panel for high pass filtered data (2 month running mean). Green: SLIMCAT; red: KASIMA; species as described in the legend.

equilibrium. For SLIMCAT the year 2000 stands out by relatively good agreement with the measurements and from 2001, coinciding with the change from ERA-40 to operational analyses, it shows increasing differences with time. The same trend, even more pronounced, is seen in KASIMA.

As already mentioned above it seems that the models are able to simulate transport processes occurring on short timescales, like tropical streamers, but perform less well in reproducing the general or long-term dynamics. For a further investigation of this issue the modelled and measured mixing ratios are correlated, before and after passing an high-pass filter. For an high-pass filter a 2-month running mean is applied, which assures that the filtered data only contain variations which take place on timescales shorter than 2 months. These analyses are made with the SLIMCAT data ranging over the whole period presented here and with KASIMA data from January 2001 onward, since at the end of 2000 this model shows strong differences due to the close initialization date. The mixing ratios are analysed for altitudes where the retrieval is especially sensitive to variabilities in the real atmosphere. It was required that the correlation between the retrieved and real atmospheric mixing ratios reaches at least a coefficient of 0.7. This minimizes the influences of the retrievals' constraints on the correlation between retrieved and modelled mixing ratios. An influence, which is the larger the less sensitive the retrieved ratios are to variabilities in the real atmosphere, i.e. the lower the coefficients of Sect. 2.4 are. Table 4 lists these retrieved altitudes, their corresponding real atmospheric 0.5$\rho$-layer, and altitude which contributes mostly to variations in the retrieved mixing ratio. The $O_3$ amounts retrieved at 37.3 km are additionally anti-correlated to their real amounts around 25 km, which complicates their interpretation.

The upper panel of Fig. 14 depicts the correlation coefficient between the unfiltered measured and modelled mixing ratios versus the real atmospheric height. The error bar indicate the 0.5$\rho$-layer. In particular for SLIMCAT it is evident that the model correlates better to the measurements in the lower stratosphere than in the middle stratosphere. For KASIMA this altitude dependence becomes visible if one considers each species separately. All species for which this analysis is performed at various altitudes tend to correlate better at lower than at higher altitudes. High-pass filtering of the measured and modelled data improves their correlation significantly (see lower panel of Fig. 14), which demonstrates that the models are well-suited in tracking atmospheric variabilities on small timescales. Only the chemically more active species $O_3$ and HCl maintain coefficients of below 0.65 for the middle stratosphere. They are particularly low for KASIMA. The good correlation for the $O_3$ and HF ratios retrieved above 34 km are less confident since their correlations to real atmospheric ratios are relatively small (see Table 4).

It can be concluded that in the middle stratosphere the models fail in predicting the $O_3$ and HCl amounts even on

small timescales. This inconsistency is very likely driven by the mentioned longer-term dynamical problems which affect the chemical state of the middle stratosphere.

### 4.3 SLIMCAT versus KASIMA

Over the whole period both SLIMCAT and KASIMA overestimate stratospheric $N_2O$ and $CH_4$ while underestimating $O_3$, HCl, and HF. An examination of the temporal evolution of their differences to the measurements, indicates that the simulation of vertical transport is too strong, resulting in strongly increasing altitudes of tracer isopleths. This feature is more pronounced in KASIMA (see e.g. the 1.6 ppmv line in Fig. 13) than in SLIMCAT. The latter only shows a weak tendency of increasing altitude of isopleths from 2001 onward. Both models use ECMWF analyses, but the way in which vertical transport is calculated differs between the models. KASIMA calculates the vertical wind from the divergence of the horizontal wind on isobaric levels, while SLIMCAT, in the run used here, uses isentropic levels in the stratosphere and calculates the vertical (diabatic) motion using the MIDRAD radiation scheme. Age-of-air tests with SLIMCAT show that using divergence/isobaric levels in this model also gives a much faster rate of vertical transport (not shown). In the past the SLIMCAT model has been used successfully for decadel simulations using UK Met Office analyses. The SLIMCAT run used here started in 1989 and simulated the period up to 2003 in a stable manner (though with some changes possibly linked to the change from ERA-40 to operational winds in early 2000). It seems that this formulation enables SLIMCAT to calculate the long-term stratospheric transport in a more realistic way than the isobaric level KASIMA model in the CTM mode.

Largest differences between the models are seen for HCl. While stratospheric column amounts are too large in KASIMA, SLIMCAT reasonably reproduces them (see Fig. 10, top). Both models overestimate HCl in the upper troposphere and lower stratosphere (UT/LS). This is less pronounced for SLIMCAT, where it is counterbalanced by the simultaneous underestimation of HCl in the middle stratosphere. For KASIMA, on the other hand, the overestimation in the UT/LS is increased by an incorrect initialisation and a slight overestimation of the total release of chlorine from the CFCs in the UT/LS (Kirner, 2004). Thus it cannot be counterbalanced by the slight underestimation of middle stratospheric values. Due to this problem the KASIMA run was stopped in early 2003.

## 5 Summary and conclusions

The unique five-year record of trace gas profiles obtained by the FTIR technique reveals the seasonal and interseasonal evolution of dynamics and chemistry of the subtropical atmosphere. The observations show enhanced upward motion in the summer and relatively strong variabilities in winter. The comparisons to long-term runs of 3-D CTMs indicate that processes on shorter timescales are well modelled, in particular in the lower stratosphere. However, the modelled long-term or general transport processes are not fully consistent with the measurements. The model/observation differences are generally larger during winter and smaller in summer, with the exception of middle stratospheric ozone, which is, in particular, underestimated in summer. A prime reason is very likely errors in the applied meteorological analysis, although further investigation is necessary to exclude definitively errors in chemical processes. Due to the interaction of dynamical and chemical processes the models show particular problems in characterizing the middle stratosphere, where chemistry occurs relatively fast.

*Acknowledgements.* We thank the Bundesministerium für Bildung und Forschung via the DLR by contracts 50EE0008 and 50EE0203 for funding. Furthermore, we are grateful to the Izaña Observatory for use of its infrastructure and to the Goddard Space Flight Center for providing the temperature and pressure profiles of the National Centers for Environmental Prediction via the automailer system used for inversion. The SLIMCAT modelling was supported by the UK Natural Environment Research Council.

Edited by: J. Burrows

## References

Brewer, A. W.: Evidence for a world circulation provided by the measurements of helium and water vapor distribution in the stratosphere, Q. J. R. Meteorol. Soc., 75, 351–363, 1949.

Chipperfield, M. P.: Multiannual Simulations with a Three-Dimensional Chemical Transport Model, J. Geophys. Res., 104, 1781–1805, 1999.

Dobson, G. M. B.: Origin and distribution of polyatomic molecules in the atmosphere, Proc. R. Soc. London Ser. A, 236A, 187–193, 1956.

European Union: European Research in the Stratosphere: Advances in our understanding of the ozone layer during THESEO, Report EUR 19867, 2001.

Hase, F., Blumenstock, T., and Paton-Walsh, C.: Analysis of the instrumental line shape of high-resolution Fourier transform IR spectrometers with gas cell measurements and new retrieval software, Appl. Opt., 38, 3417–3422, 1999.

Hase, F., Hannigan, J. W., Coffey, M. T., Goldman, A., Höpfner, M., Jones, N. B., Rinsland, C. P., and Wood, S. W.: Intercomparison of retrieval codes used for the analysis of high-resolution, ground-based FTIR measurements, J. Quant. Spectrosc. Radiat. Transfer, 87, 25–52, 2004.

Höpfner, M., Stiller, G. P., Kuntz, M., v. Clarmann, T., Echle, G., Funke, B., Glatthor, N., Hase, F., Kemnitzer, H., and Zorn, S.: The Karlsruhe optimized and precise radiative transfer algorithm, Part II: Interface to retrieval applications, SPIE Proceedings 1998, 3501, 186–195, 1998.

Kirner, O.: Bewertung und Validierung einer mehrjährigen KASIMA-Simulation durchgeführt mit ERA-40 Reanalysen, Diploma Thesis, University of Karlsruhe, Germany, 2004.

Kouker, W., Langbein, I., Reddmann, Th., and Ruhnke, R.: The Karlsruhe Simulation Model of the Middle Atmosphere (KASIMA), Version 2, FZK report 6278, Forschungszentrum Karlsruhe, Germany, 1999.

Kuntz, M., Höpfner, M., Stiller, G. P., v. Clarmann, T., Echle, G., Funke, B., Glatthor, N., Hase, F., Kemnitzer, H., and Zorn, S.: The Karlsruhe optimized and precise radiative transfer algorithm, Part III: ADDLIN and TRANSF algorithms for modeling spectral transmittance and radiance, SPIE Proceedings 1998, 3501, 247–256, 1998.

Lary, D. J. and Toumi, R.: Halogen-catalyzed methane oxidation, J. Geophys. Res., 102, 23 421–23 428, 1997.

Rodgers, C. D.: Inverse Methods for Atmospheric Sounding: Theory and Praxis, World Scientific Publishing Co., Singapore, 2000.

Rothman, L. S., Barbe, A., Benner, D. C., Brown, L. R., Camy-Peyret, C., Carleer, M. R., Chance, K. V., Clerbaux, C., Dana, V., Devi, V. M., Fayt, A., Fischer, J., Flaud, J.-M., Gamache, R. R., Goldman, A., Jacquemart, D., Jucks, K. W., Lafferty, W. J., Mandin, J.-Y., Massie, S. T., Newnham, D. A., Perrin, A., Rinsland, C. P., Schroeder, J., Smith, K. M., Smith, M. A. H., Tang, K., Toth, R. A., Vander Auwera, J., Varanasi, P., and Yoshino, K.: The HITRAN Molecular Spectroscopic Database: Edition of 2000 Including Updates through 2001, J. Quant. Spectrosc. Radiat. Transfer, 82, 5–44, 2003.

Ruhnke, R., Weiss, C., Reddmann, T., and Kouker, W.: A comparison of multiannual CTM calculations using operational and ERA-40 ECMWF analyses, Contributions to EGS, Nice, 2003.

Schneider, M.: Continuous Observations of Atmospheric Trace Gases by Ground-based FTIR Spectroscopy at Izaña Observatory, Tenerife Island, Scientific Reports Forschungszentrum Karlsruhe, FZKA 6727, ISSN 0947-8620, 2002.

Schneider, M., Blumenstock, T., Hase, F., Höpfner, M., Cuevas, E., Redondas, A., and Sancho, J. M.: Ozone Profiles and Total Column Amounts derived at Izaña, Tenerife Island, from FTIR Solar Absorption Spectra, and its Validation by an Intercomparison to ECC-Sonde and Brewer Spectrometer Measurements, J. Quant. Spectrosc. Radiat. Transfer, 91, 245–274, 2005.

Stiller, G. P., Höpfner, M., Kuntz, M., v. Clarmann, T., Echle, G., Fischer, H., Funke, B., Glatthor, N., Hase, F., Kemnitzer, H., and Zorn, S.: The Karlsruhe optimized and precise radiative transfer algorithm, Part I: Requirements, justification and model error estimation, SPIE Proceedings 1998, 3501, 257–268, 1998.

Trepte, C. R. and Hitchman, M. H.: Tropical stratospheric circulation deduced from satellite aerosol data, Nature, 355, 626–628, 1992.

Wagner G., Birk, M., Schreier, F., and Flaud, J.-M.: Spectroscopic database for Ozone in the fundamental spectral regions, J. Geophys. Res., 107, 4626–4643, 2002.

World Meteorological Organization (WMO): Scientific Assessment of Ozone Depletion: 2002, Global Ozone Research and Monitoring Project – Report No. 47, Geneva, 2003.